ORIGINAL ARTICLE

Drug nanoclusters formed in confined nano-cages of CD-MOF: dramatic enhancement of solubility and bioavailability of azilsartan ☆

Yuanzhi He[a,b,†], Wei Zhang[b,c,†], Tao Guo[b,†], Guoqing Zhang[b,†],
Wei Qin[a,b], Liu Zhang[b], Caifen Wang[b], Weifeng Zhu[a], Ming Yang[a],
Xiaoxiao Hu[b], Vikramjeet Singh[d], Li Wu[b,e,***], Ruxandra Gref[d,**],
Jiwen Zhang[a,b,c,e,*]

[a]Key Laboratory of Modern Preparation of TCM, Ministry of Education, Jiangxi University of Traditional Chinese Medicine, Nanchang 330004, China
[b]Center for Drug Delivery Systems, Shanghai Institute of Materia Medica, Chinese Academy of Sciences, Shanghai 201210, China
[c]School of Chemistry and Environmental Engineering, Shanghai Institute of Technology, Shanghai 201418, China
[d]Institut des Sciences Moléculaires d'Orsay, UMR 8214 CNRS, Université Paris-Sud, Université Paris-Saclay, Orsay 91400, France
[e]School of Pharmacy, Key Laboratory of Molecular Pharmacology and Drug Evaluation, Ministry of Education, Yantai University, Yantai 264005, China

Abstract Tremendous efforts have been devoted to the enhancement of drug solubility using nanotechnologies, but few of them are capable to produce drug particles with sizes less than a few nanometers. This challenge has been addressed here by using biocompatible versatile γ-cyclodextrin (γ-CD) metal-organic framework (CD-MOF) large molecular cages in which azilsartan (AZL) was successfully confined producing clusters in the nanometer range. This strategy allowed to improve the bioavailability of AZL in Sprague–Dawley rats by 9.7-fold after loading into CD-MOF. The apparent solubility of AZL/CD-MOF was enhanced by 340-fold when compared to the pure drug. Based on molecular modeling, a dual molecular mechanism of nanoclusterization and complexation of AZL inside the CD-MOF cages was proposed, which was confirmed by small angle X-ray scattering (SAXS) and

*Corresponding author. Tel./fax: +86-21-20231980.
**Corresponding author. Tel./fax: +33-0-169158247.
***Corresponding author. Tel./fax: +86-0-20231980.
  E-mail addresses: track_wuly@163.com (Li Wu), ruxandra.gref@u-psud.fr (Ruxandra Gref), jwzhang@simm.ac.cn (Jiwen Zhang).
†These authors made equal contributions to this work.
☆Invited for Special Column.

synchrotron radiation-Fourier transform infrared spectroscopy (SR-FTIR) techniques. In a typical cage-like unit of CD-MOF, three molecules of AZL were included by the γ-CD pairs, whilst other three AZL molecules formed a nanocluster inside the 1.7 nm sized cavity surrounded by six γ-CDs. This research demonstrates a dual molecular mechanism of complexation and nanoclusterization in CD-MOF leading to significant improvement in the bioavailability of insoluble drugs.

1. Introduction

As one of the most investigated areas of innovative crystalline highly porous materials, metal-organic frameworks (MOFs) are structurally versatile materials comprised of inorganic and organic components[1–4]. Owing to their large surface area, tunable structure functionalization and porosity, MOFs are being explored for a wide variety of potential applications such as sensing[5,6], gas storage[7,8], chromatographic separation[9,10], catalysis[11], template synthesis[12], and drug delivery[13,14]. Most of MOFs are composed of metals (i.e., Co, Ni, Cr, and Gd), which are toxic in view of potential biological applications[15], and the available data on organic ligands and their biological fate are limited[16,17]. Thus, MOFs composed of pharmaceutical excipients and endogenous metal ions are of great interest for the design of drug delivery system[18,19]. Recently, γ-cyclodextrin metal-organic framework (CD-MOF) is considered as a green, renewable framework material, linked by coordination of the secondary face hydroxyl groups on alternating D-glucopyranosyl residues to one of the alkali metal cations to form body-centered cubic extended structures[20]. In the unit cell of CD-MOF, six γ-CDs constitute six sides of the cube. Porous CD-MOF has two main kinds of cages in the molecular structure: i) spherical voids with diameter of 1.7 nm formed by six γ-CDs, and ii) cavities with diameter of 0.8 nm formed by face to face γ-CD pairs. Taking advantage of the interconnected channels, the large spherical voids can serve as confined nanoreactors[21]. The reaction products formed in these confined spaces exhibit the desired uniform size distributions which are hard to be achieved by conventional methods[22,23]. Several successful reports have been published on drug loading into CD-MOF[24,25], but the mechanism of drug loading could neither be simply interpreted as adsorption[26], encapsulation[27], inclusion nor co-crystallization[25]. Herein, to further probe the mechanism of drug loading in CD-MOF, a water insoluble drug, namely, azilsartan (AZL) was selected as a model hydrophobic drug.

AZL is the latest angiotensin II receptor blocker (ARB) for the treatment of hypertensions[28]. Compared with olmesartan and valsartan, AZL has superior efficacy at its maximal dose[29] for its high binding to and slow dissociation from AT1 receptors[30]. AZL is insoluble in water and its solubility is pH-dependent[31]. The absorption site of AZL is mostly in the upper parts of small intestine and is poorly absorbed by the stomach and colon[32,33]. Therefore, it is of great interest to enhance the solubility and the bioavailability of AZL. A number of strategies have been applied to improve the solubility of poorly water soluble drugs[34–36] such as particle size reduction[37], prodrugs[38], liposomes[39], solid dispersions[40] and cyclodextrins inclusion compounds[41]. However, the majority of the literatures about AZL are focused on its antihypertensive efficacy and safety[42–45], whilst there are very few investigations on the solubility improvement of AZL[31,46].

CD-MOF was used here as a carrier to improve the solubility and oral bioavailability of AZL. The nanometer-sized CD-MOF was successfully synthesized and conveniently loaded with AZL by agitation. AZL was loaded into two kinds of molecular cages in CD-MOF following different drug loading mechanisms. One mechanism consists in encapsulation in γ-CD pairs and the other one is the confinement of AZL molecules in nanometer-sized cage-like spaces. Therefore, both experimental and simulation studies were performed to assess the location of AZL inside CD-MOF and more particularly, to evidence the presence of AZL nanoclusters in confined large cages in CD-MOF. The oral bioavailability of AZL loaded in CD-MOF (AZL/CD-MOF) was compared with that of included by γ-CD (AZL/γ-CD) and pure AZL in fasted male Sprague–Dawley rats. Overall, the obtained results suggested that the nanoclusters played a key role in the solubility and bioavailability enhancement of AZL/CD-MOF.

2. Materials and methods

2.1. Materials

AZL was provided by Zhejiang Guobang Pharmaceutical Co., Ltd. (Zhejiang, China). γ-CD was obtained from Maxdragon Biochem Co., Ltd. (Guangdong, China). Methanol (MeOH), potassium hydroxide (KOH), polyethylene glycol 20,000 (PEG20000), ethanol (EtOH), glacial acetic acid and other reagents of analytical grade were all purchased from Sinopharm Chemical Reagent Co., Ltd. (Shanghai, China) and used without further purification. Water was purified by passing through a reverse osmosis unit of a Milli-Q reagent water system (Millipore, France).

2.2. Loading of AZL into CD-MOF and γ-CD

The synthetic protocol for CD-MOF was adopted from our reported procedure and included in the Supporting Information[26]. The AZL loading profile was investigated using a simple agitation approach. AZL was loaded into CD-MOF under magnetic agitation (RCT IKA, Staufen, Germany) under incubation with ethanol solution of AZL for 24 h. Briefly, 300 mg of dried CD-MOF powder was dispersed into 20 mL of EtOH solution of AZL with the final concentration of 13 mg/mL (molar ratio of γ-CD in CD-MOF to AZL was 1:3) and agitated at 40 °C with a speed of 50 rpm. The precipitates were collected by centrifugation and dried under vacuum overnight to obtain AZL/CD-MOF.

Inclusion complex of γ-CD and AZL in 2:1 molar ratio was prepared by ball milling method using a high-energy impacting grinder (CJM-SY-A, Qinhuangdao Taiji Ring Nano-Products Co., Ltd., China). AZL and γ-CD were separately sieved through 100

mesh sieve, weighed and mixed in the above-mentioned ratio. The zirconia beads milling was charged first with zirconia beads (11 mm average diameter, weight of zirconia beads and the mixed powder was 10:1 w/w) and then blended with the powders. To enhance the efficiency of the inclusion process, three-fold amount of water and ethanol in 1:1 ratio (v/v) was added. The obtained product was dried overnight under vacuum at 50 °C. The optimum milling time was studied, which was found to be 2 h. The final product was kept in airtight container till further analysis. Physical mixture (PM) of AZL and γ-CD was prepared by mixing the powders in geometric proportion.

2.3. Quantification of AZL

The amount of AZL was determined by high performance liquid chromatography with UV detection (HPLC-UV, Agilent 1290, Agilent Technologies, USA). Analysis was carried out with a C18 column (250 mm × 4.6 mm, 5 µm, Dikma, USA) operating at 30 °C. The mobile phase was composed of acetonitrile, water and glacial acetic acid (50:50:1, $v/v/v$) delivered at 1.0 mL/min. Analyses were carried at 254 nm wavelength with 20 µL injection volume. Data were collected by Chemstation version B.04.03 software (Agilent Technologies, USA). In these conditions, the drug retention time ranged within 7.2–7.5 min. Effective drug contents were calculated from a linear calibration curve ($r = 0.9999$) established in the 0.25 to 100 µg/mL concentration range.

AZL loading was measured by dissolving 5 mg of sample in 10 mL of water and methanol solvent (1:1, v/v), the centrifuged solution was analyzed by HPLC-UV. The presence of CD-MOF did not interfere with the HPLC analysis of the drug. The AZL loading percentage was calculated according to the following Eq. (1):

$$\text{AZL loading}(\%) = \frac{\text{AZL determined in CD} - \text{MOF}}{\text{Weight of AZL / CD} - \text{MOF}} \times 100 \qquad (1)$$

2.4. Solubility study

Apparent solubility of AZL/CD-MOF in different media including hydrochloric acid solution (pH 1.2), acetate buffer (pH 4.5), phosphate buffer (pH 6.8), and distilled water were determined by the shake-flask method. Excess amounts of AZL, AZL/γ-CD and AZL/CD-MOF were added to 5 mL of different medium in screw-capped glass vials, then mechanically shaken (ES-60+, Wiggens, Germany) at 25 °C for 72 h. Followed by filtration with a syringe filter (filter HA-0.45 µm, Millipore) to remove the insoluble solids. The filtrate was diluted with each media and analyzed by HPLC. Each experiment was performed in triplicates, the coefficient of variation (CV) associated with each measurement was less than 3%.

2.5. In vitro dissolution studies

In vitro dissolution performance was estimated using an USP II dissolution apparatus (Model 2500, Distek Co., USA). Forty mg raw AZL, equivalent AZL/γ-CD and AZL/CD-MOF solid systems were placed to 900 mL media (pH 1.0 HCl solution, pH 4.5 acetate buffer, pH 6.8 phosphate buffer, and distilled water) at 37 °C and at a paddle rotating speed of 50 rpm, respectively. An aliquot of 5 mL was withdrawn at 3, 5, 10, 15, 20, 30, 45 and 60 min, filtered through a 0.22 µm membrane, and the removed volume was replaced with 5 mL of fresh medium. Then, the concentration of

AZL was estimated by HPLC method. The dissolution was measured in triplicates for each sample, and the mean cumulative dissolution profile was plotted.

2.6. Scanning electron microscopy (SEM)

Morphological characterizations were conducted using an SEM (S3400, Hitachi, Japan). Specimens were immobilized on metal stubs with double-sided adhesive tape and coated with gold, then observed under definite magnification.

2.7. Powder X-ray diffraction (PXRD)

Crystallinity of the samples was characterized by PXRD. Diffraction patterns were detected with a Bruker D8 Advance diffractometer (Bruker, USA). Samples were irradiated with monochromatized Cu K$_\alpha$ radiation ($\lambda = 1.54$ Å) and analyzed over a 2θ angle range of 3–40° with a tube voltage of 40 kV, a tube current of 40 mA at a scan speed of 0.1 s/step.

2.8. Synchrotron radiation Fourier transform infrared spectroscopy (SR-FTIR)

SR-FTIR spectra of samples were obtained in Shanghai Synchrotron Radiation Facility (SSRF) using a spectrometer (Nicolet 6700, Thermo Scientific, USA). Sample was thoroughly mixed with potassium bromide and compressed into a tablet. Each specimen was recorded with 128 scans at a resolution of 4 cm^{-1} in a wavenumber range of 400–4000 cm^{-1}.

2.9. Nitrogen adsorption isotherm

Nitrogen adsorption–desorption isotherm was measured with a liquid nitrogen bath (-196 °C) using a porosimeter (Micromeritics ASAP 2020, USA). Before test, samples were vacuum dried at 50 °C for 12 h to remove residual solvent and moisture.

2.10. Differential scanning calorimetry (DSC)

Calorimetric measurements were carried out with a differential scanning calorimeter (PerkinElmer DSC8500, USA) in the temperature range from 25 to 300 °C with a heating rate of 10 °C/min under constant nitrogen purging of 30 mL/min. Calibrations for the temperature and enthalpy were achieved from measurements of melting temperature and enthalpy of indium ($T_m = 156.6$ °C and $\Delta H_m = 28.5$ J/g).

2.11. Small angle X-ray scattering (SAXS)

SAXS experiments were performed on a SAXSess mc2 nanostructure analyzer (Anton Paar, Austria), with an incident X-ray monochromatic beam ($\lambda_{CuK\alpha} = 1.54$ Å) monitored by a photomultiplier. The rotating anode device was operated at 50 kV and 1 mA. Scattering in the range (scattering vector $q = 4\pi\sin(\theta)/\lambda$, with λ as the wavelength and θ as half the scattering angle) of 0.01–8.53 nm^{-1} was detected. CD-MOF or AZL/CD-MOF was placed on the aluminum foil. The distance between the sample and the detector was set to 25 cm. Each SAXS pattern was accumulated for 1 h.

2.12. Molecular docking

The crystal structure of CD-MOF was extracted from the reported single crystal structure of CD-MOF-1[20]. The molecular structure of AZL was constructed manually. The molecular dynamics program of Amber 12 was employed to perform energy minimization and molecular dynamics calculation. The Amber Tools in Amber 12 was used to prepare the starting stuffs. The force field parameters of γ-CD were downloaded from GLYCAM-Web (http://glycam.org/docs/forcefield/parameters/). The partial atomic charge of the AZL was calculated employing Gaussian 09 package. The automated molecular docking program Auto Dock Vina 1.1.2 was used to generate the initial position of AZL.

Firstly, energy minimization protocol was executed to prepare AZL model. Then, the AZL molecule was docked to CD-MOF model. The docking result with the relatively low energy was used for the successive structure optimization.

In the minimization protocol, all the models were put in the vacuum. Then, a 20 ns molecular dynamic was performed. The nonbond cutoff distance of 18.5 Å, spline width of 1.0 Å and buffer width of 0.5 Å were used, respectively. In the docking protocol, a Lamarckian Genetic Algorithm (LGA) in combination with a grid-based energy evaluation method were used for pre-calculating grid maps according to the interatomic potentials of all atom types present in the host and guest molecules, including the Lennard-Jones potentials for Van Der Waals interactions and Coulomb potentials for electrostatic interactions[47]. A grid map of dimensions 30 Å × 30 Å × 30 Å with a grid spacing of 0.375 Å was placed to cover the CD-MOF model. With the help of AutoDockTools, the atomic partial charges were calculated by the Gasteiger-Marsili method[48]. The parameters used for the global search were an initial population of 50 individuals, with a maximal number of energy evaluations of 1,500,000 and a maximal number of generations of 50,000 as an end criterion. Other docking parameters were set as default.

2.13. Pharmacokinetic study

The male Sprague–Dawley rats (200 ± 20 g) were provided by Shanghai Lab Animal Research Center (Shanghai, China) and randomly divided into three groups of 6 each. All rats were fasted overnight prior to the experiment but allowed free access to water. The three groups were orally administrated with raw AZL, AZL/γ-CD and AZL/CD-MOF at a dose of 1.0 mg/kg respectively, which were dispersed in 0.5% sodium carboxymethylcellulose (CMC-Na) respectively. At pre-specified time intervals of 0, 0.08, 0.25, 0.5, 1, 1.5, 2, 4, 8, 12 and 24 h retro-orbital blood samples were collected into 1.5 mL heparinized centrifuge tubes. The tubes were immediately centrifuged (3500 rpm × 10 min, Thermo Fisher Scientific Micro 2 R, Waltham MA, USA) to collect the plasma, which was transferred to a new tube and stored frozen at −80 °C until further analysis. All animal experiments were carried out with the approval of the Institutional Animal Care and Use Committee of Shanghai Institute of Materia Medica, Chinese Academy of Sciences (IACUC Application No. 2017-05-ZJW-11, Shanghai, China).

Plasma samples were removed from −80 °C storage and kept at ambient conditions till melted. 50 μL of plasma samples spiked with 10 μL of valsartan (100 ng/mL) and 10 μL of solution (acetonitrile:water = 60:40, v/v) were vortexed for 30 s. Acetonitrile (130 μL) was then added and vortexed for 30 s. After mixing, the samples were centrifuged (12,000 rpm × 5 min) and aliquots of 10 μL supernatant were injected into the HPLC–MS/MS system.

2.14. HPLC–MS/MS analysis

Plasma samples were quantified on a highly sensitive HPLC–MS/MS system that consisted of an Agilent 1260 HPLC coupled to an Agilent G6460A triple quadrupole mass spectrometer (Agilent Technologies, Torrance, USA). The chromatographic system used consisted of a binary pump of G4220A, an auto-sampler of G4226A and a column oven of G1316C. Data were collected by MassHunter V4.1 software. AZL and internal standad (valsartan) were separated on an core-shell XB-C18 column (150 mm × 4.6 mm, 5 μm, Phenomenex, USA) at 35 °C. The mobile phase was consisted of 0.1% formic acid aqueous solution and acetonitrile (40:60,v/v) which performed at a flow rate of 0.6 mL/min. An injection volume of 10 μL was applied for analysis.

Mass spectrometric detection was performed using a jet stream electrospray ionization (ESI) source operating in the negative ion mode. The instrument was optimized for the quantification. Nitrogen was used as both the drying gas under a flow of 10 L/min at 300 °C and the sheath gas under a flow of 10 L/min at 350 °C. The pressure of nebulizer was 35 psi. The instrument was operated with a capillary voltage of 3.5 kV. Multiple reaction monitoring (MRM) transitions were employed for data acquisition with transitions of m/z 455.2→411.3 for AZL and the transitions of m/z 431.1→179.1 for valsartan.

The concentrations of AZL were calculated from a linear calibration curve established in the 2.07 to 1035.00 ng/mL concentration range. Least squares method was used to establish the standard curve of AZL with the weight of $1/x^2$. The accuracies were within 91.57%–107.50% for the blood calibration standards at all the concentration levels. The typical standard curve equations for AZL was:

$$R = 1.26 \times 10^{-2}C - 1.06 \times 10^{-2} \tag{2}$$

where R is peak area ratio of AZL to valsartan and C is concentration of AZL ($r^2 = 0.9960$).

2.15. Statistical methods

Linear regression analysis was used to verify the linearity of the calibration curves. AZL was expressed as mean ± standard deviation (SD) and examined by t-test. All statistical analyses were performed with SPSS 17.0 (SPSS Inc., Chicago, IL, USA). The pharmacokinetic parameters of analyses were calculated by the non-compartmental analysis using the DAS 2.0 software. P values of <0.05 or <0.01 were considered to be statistically significance.

3. Results and discussion

3.1. Highly efficient loading and dramatically improved solubility of AZL

AZL was incorporated by simply immersing the CD-MOF crystals into AZL ethanolic solution (13 mg/mL) by agitation and incubation at 40 °C. As shown in Fig. 1A, the ostensive equilibrium reached within 8 h of incubation. AZL loading to CD-MOF reached 22.8 ± 0.6% (w/w) corresponding to a molar ratio of AZL to γ-CD in CD-MOF of around 1:1 calculated by the
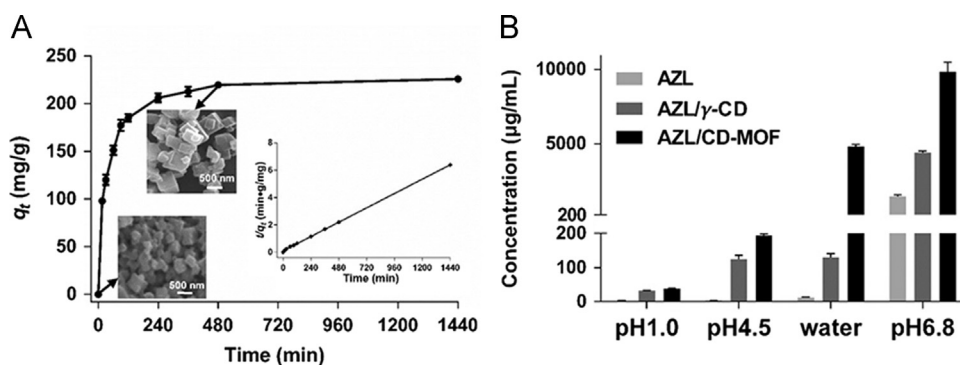
Figure 1 Highly efficient loading and dramatically improved solubility of AZL achieved by CD-MOF. (A) Effect of the incubation time on the loading efficiency of AZL (13 mg/mL) into CD-MOF ($n = 3$) with corresponding SEM images of CD-MOF, AZL/CD-MOF and the fitting of the pseudo-second-order kinetics. (B) Dramatically enhanced solubility of AZL/CD-MOF compared with AZL and AZL/γ-CD at different pH values.

corresponding amount of CD-MOF converted into CD versus the moiety of AZL loaded. Of note, such loadings could not be achieved *via* conventional complexation processes. The AZL loading rate fitted well in a pseudo-second-order kinetic model ($R^2 = 0.9999$) of t/q_t against time (Fig. 1A). Taking into account the molecular bonds rotation and stretching, the windows dimensions of γ-CD (0.8 nm) and the internal cavities in CD-MOF (1.7 nm) are compatible with the molecular dimensions of AZL molecules which is 0.89 nm × 1.61 nm. After AZL loading, AZL/CD-MOF particles were colorless and maintained their original morphology and crystalline structure. This finding was a preliminary presumption of the efficient incorporation of AZL into CD-MOF.

Solubility is one of the essential parameters considered in the pre-formulation phase. As indicated in Fig. 1B, the apparent solubility of AZL/CD-MOF in water was enhanced 340-fold compared to raw AZL. On the contrary, an only 9.4-fold increment was recorded when forming γ-CD inclusion complexes by ball

milling method with the molar ratio of 1:2 for AZL and γ-CD. Overall, AZL/CD-MOF showed higher solubility than AZL/γ-CD and raw AZL in all the tested pH range from 1.0 to 6.8.

3.2. Enhanced dissolution rate in vitro

In order to improve the oral bioavailability of poorly water-soluble drugs, it is indispensable to study the *in vitro* dissolution behaviors of the formulations. As illustrated in Fig. 2, the dissolution profiles of raw AZL displayed pronounced pH-dependent behavior due to its weak acidic nature and low dissolution rate at lower pH values. Only less than 10% of AZL dissolved within 60 min in pH 1.0 HCl solution, pH 4.5 acetate buffer and distilled water. In contrast a dramatic increase in both the dissolution rate and extents were observed with AZL/CD-MOF, as more than 90% of the drug was dispersed within 3 min in pH 6.8 phosphate buffer and in distilled water. In pH 4.5 acetate buffer, $45.54 \pm 3.55\%$ of AZL was dissolved from AZL/CD-MOF at 60 min and $29.64 \pm 0.55\%$ of
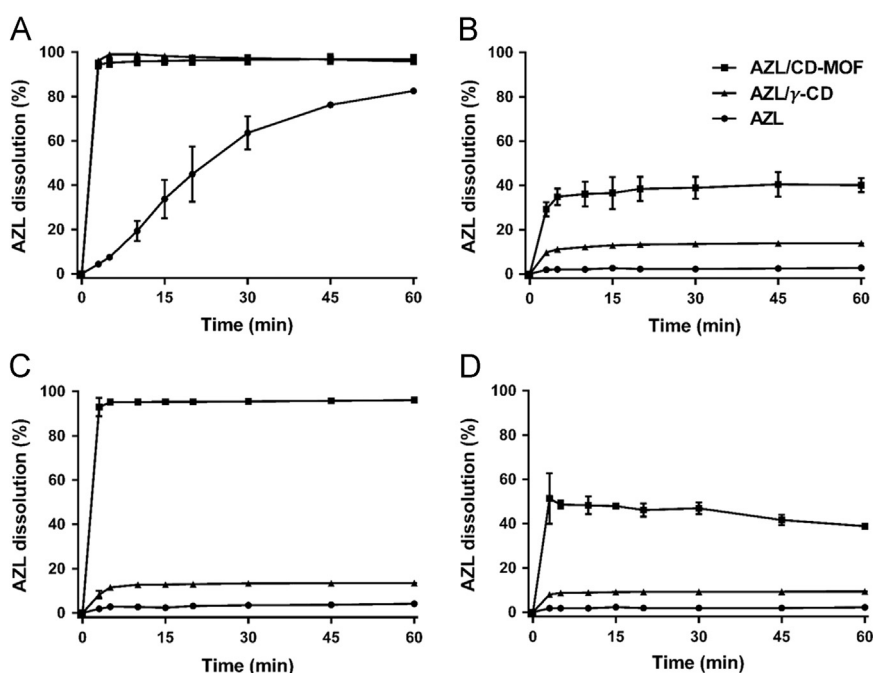

Figure 2 Dissolution profiles of AZL/CD-MOF, AZL/γ-CD and AZL in pH 6.8 phosphate buffer (A), pH 4.5 acetate buffer (B), distilled water (C) and pH 1.0 HCl solution (D). Each value represents the mean $\pm$ SD ($n = 3$).

AZL was dissolved at the same time in pH 1.0 HCl solution. However, it is worthy to mention that at the 30 min dissolution, the AZL dissolved from AZL/CD-MOF in pH 1.0 HCl solution is faster than that in pH 4.5 acetate buffer, it is possible that the dissolution rate in low ion concentration solution is faster than that in high ion concentration buffer and the AZL nanoclusters released from CD-MOF structure in pH 1.0 HCl solution precipitated at the endpoint of the dissolution. For AZL/γ-CD, although the dissolution rate has been ameliorated contrasted to raw AZL to a certain degree, but the improvement in apparent solubility was quite limited in comparison to AZL/CD-MOF in all tested dissolution media except in pH 6.8 phosphate buffer. Compared with the dissolution rate of AZL/γ-CD and raw AZL, AZL/CD-MOF has the overwhelming superiority in pH 1.0 HCl solution and pH 4.5 acetate buffer. The arresting apparent solubility improvement of AZL when using AZL/CD-MOF may be attributable to the typical supramolecular organization of γ-CDs in CD-MOF. It is expected that such an increase in apparent solubility could upgrade the *in vivo* bioavailability of AZL.

3.3. Enhanced bioavailability in rats

Oral delivery of AZL is challenging because of its poor solubility in aqueous and physiological environments. To some extent, both γ-CD and CD-MOF could ameliorate the solubility of hydrophobic active pharmaceutical ingredient (API), while the difference in bioavailability is always unknown. The plasma concentration-time profiles of same dose of AZL in male rats following oral administration have shown significant absorption enhancement after loading into the CD-MOF. After oral administration of AZL/CD-MOF, plasma concentration of AZL increased rapidly and reached a maximum concentration within 1.5 h, which was
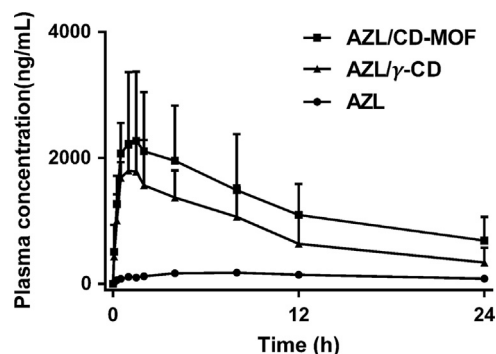

Figure 3 Plasma concentration-time profiles of AZL in rats after orally administrated AZL/CD-MOF, showing significant bioavailability improvement in comparison to AZL/γ-CD and AZL ($n = 6$, mean$\pm$SD).

remarkably ahead of raw AZL (Fig. 3). The relative bioavailability of the group treated with AZL/CD-MOF was found nearly 9.7-fold higher than that of AZL administered as free drug and 1.5-fold higher than that of AZL/γ-CD (Table 1). The results demonstrated that CD-MOF was effective in enhancing the AZL release as well as the *in vivo* absorption, which strongly indicated that AZL loading in CD-MOF occurs not only by γ-CD inclusion but other different mechanisms existed. Thus, an in depth characterization has been carried out to investigate the mechanism by which AZL/CD-MOF increase by an extra 1.5-fold the bioavailability of AZL as compared to AZL/γ-CD.

3.4. Characterization of AZL/CD-MOF

The powder X-ray diffraction (PXRD) patterns of both AZL and CD-MOF showed its own intrinsic peaks at the diffraction angles of their typical crystalline pattern (Fig. 4A). After AZL loading into CD-MOF, the intrinsic peaks of AZL crystals disappeared and the intensity of the remaining CD-MOF peaks was weakened. The weakened diffraction peaks of CD-MOF could be due to that slight γ-CD leak from CD-MOF in ethanol during the loading agitation approach[24], and the hypothesis was inferred by SR-FTIR investigations. The characteristic wide band at $2926\,\mathrm{cm}^{-1}$ assigned to –CH– (ν_{CH}) vibrations in CD-MOF decreased to some extent and the stretching vibration brand of the hydroxyl group at 3000–$3600\,\mathrm{cm}^{-1}$ was broader after the agitation approach. The disappearance of AZL crystals intrinsic peaks indicated that the AZL inside CD-MOF lost its original crystalline form and transformed the crystalline into amorphous state after drug loading process. Similarly, no peak was observed in AZL/γ-CD due to an amorphous structure of AZL encapsulated in γ-CD.

The changes in the bonding between functional groups could be observed through SR-FTIR (Fig. 4B). SR-FTIR spectra of AZL alone showed two distinctive carbonyl absorption bands at 1775 and $1693\,\mathrm{cm}^{-1}$, assigned to the carboxyl carbonyl and amide carbonyl stretching, respectively. These bands are of diagnostic value to elucidate the interactions between AZL and CD-MOF. The two absorption bands of AZL appeared unchanged in its physical mixture. On the contrary, the signals of carboxyl carbonyl and amide carbonyl band in AZL/CD-MOF were shifted to 1770 and $1646\,\mathrm{cm}^{-1}$, respectively, which is believed to arise from the spectral shift of carbonyl groups in AZL, highlighting the strong interaction between the carrier and drug molecules, involving hydrogen bonds and electrostatic attraction. On the other hand, the signal of carboxyl carbonyl band in AZL/γ-CD was unchanged and the amide carbonyl shifted to $1640\,\mathrm{cm}^{-1}$, which demonstrated the host-guest interaction between AZL and γ-CD. Similarly, the two absorption bands of AZL and γ-CD physical mixture appeared unchanged. SR-FTIR spectra illustrated the interaction between

Table 1 Pharmacokinetic parameters of AZL/CD-MOF, AZL/γ-CD and AZL in rats.

Parameter	AZL/CD-MOF	AZL/γ-CD	AZL
AUC$_{(0\text{-}24\,h)}$ (μg/mL h)	30.65 ± 14.24[**]	20.43 ± 7.66[**]	3.16 ± 0.42
T_{max} (h)	1.50 ± 1.30[**]	0.92 ± 0.38[**]	6.67 ± 2.07
C_{max} (μg/mL)	2.63 ± 1.02[**]	2.03 ± 0.38[**]	0.19 ± 0.01

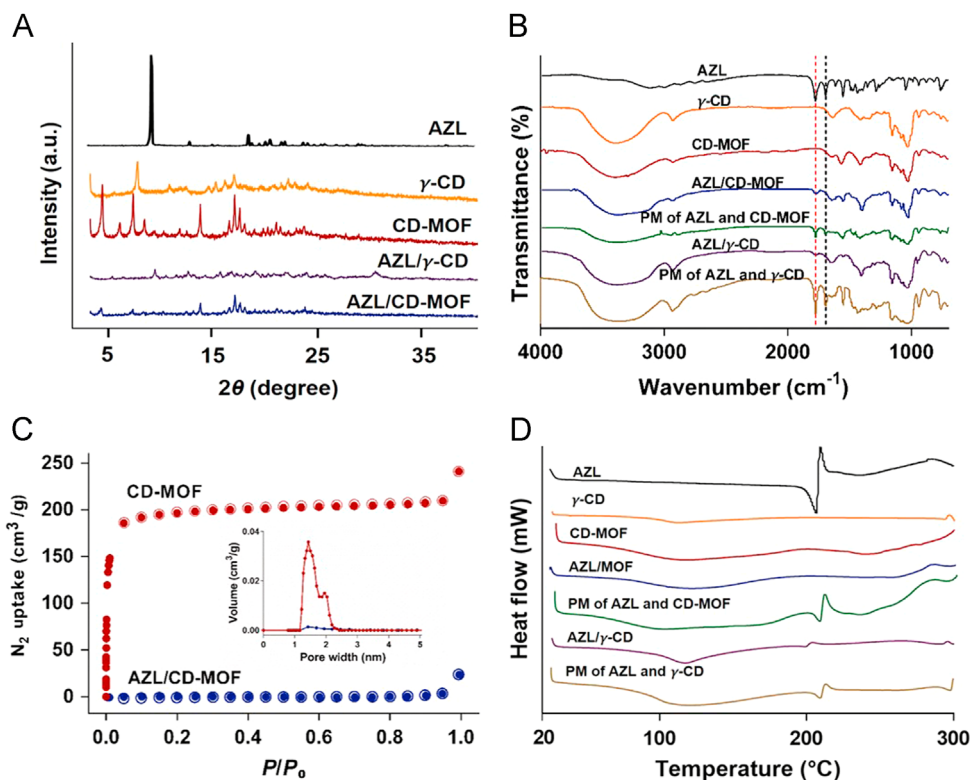Data are mean$\pm$SD, $n = 6$.
[**]$P < 0.01$ *versus* AZL.

Figure 4 Characterizations of AZL, CD-MOF, AZL/CD-MOF and AZL/γ-CD. (A) PXRD patterns, (B) SR-FTIR spectra, (C) N_2 adsorption-desorption isotherms (P/P_0, relative pressure) and pore width distribution of CD-MOF and AZL/CD-MOF (insert) (D) DSC thermograms of AZL, CD-MOF, AZL/CD-MOF, AZL/γ-CD and its equimolar physical mixture (PM).
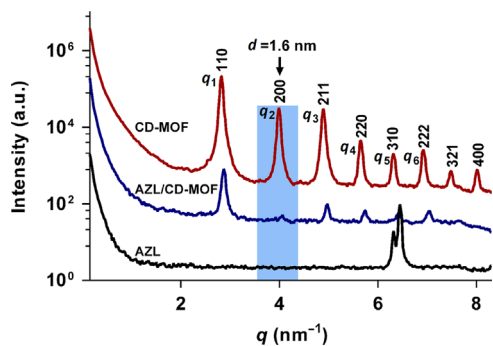

Figure 5 SAXS scattering curve of AZL, CD-MOF and AZL/CD-MOF. After AZL loading in CD-MOF, the SAXS scattering signal of AZL/CD-MOF at q_2 disappeared, suggesting an occupation of the large CD-MOF cavities with a diameter of 1.6 nm by AZL molecules.

AZL and γ-CD in CD-MOF is different from that of γ-CD inclusion complex.

AZL loading led to a significant decrease in the N_2 uptake of CD-MOF (Fig. 4C), which further proved that the interconnected pores were occupied by AZL. Indeed, for blank CD-MOF, the Langmuir surface area was recorded as 996 m^2/g. In contrast, the Langmuir surface area of AZL/CD-MOF was estimated near 0 m^2/g, indicating that almost no residual porosity was left in AZL/CD-MOF crystals after drug loading. Pore width distribution curves of CD-MOF and AZL/CD-MOF were shown in Fig. 4C (insert). The pore size of CD-MOF was in the range of 0.5–2.0 nm and the mean pore width was a little bit less than the thearetical size (1.4 nm) using the density functional theory (DFT) calculation on nitrogen adsorption in CD-

MOF. After AZL loading, the dramatically decreased pore volume of CD-MOF from 0.038 to 0 cm^3/g directly demonstrated that AZL occupied the pores in CD-MOF.

DSC was employed to gain information on the physical state of AZL in AZL/CD-MOF as compared to AZL/γ-CD, using as reference free drug and empty CD-MOF as well as related physical mixtures (Fig. 4D). As expected, an endothermic peak appeared at 205 °C in the DSC curve of the raw AZL, corresponding to its melting point and indicating its crystalline nature. At the same time, no such peak was observed in both of CD-MOF and γ-CD in the same tested range of 25–300 °C. Compared to the raw AZL, both the physical mixtures of AZL with CD-MOF or γ-CD showed unchanged melting point. In contrast, the endothermic peak of AZL completely disappeared from AZL/CD-MOF and AZL/γ-CD, indicating profound changes of the original crystal features of AZL in CD-MOF and γ-CD.

3.5. Small angle X-ray scattering

SAXS can provide high-resolution scattering profiles for systems and events occurring at a wide scale range (1–200 nm)[49,50]. In this study, SAXS was performed to further investigate the drug distribution in CD-MOF. As can be seen from the pattern of CD-MOF (Fig. 5), the peaks appeared with relative positions of q_1:q_2:q_3:q_4:q_5:q_6, etc. = 1: $\sqrt{2}$: $\sqrt{3}$: $\sqrt{4}$: $\sqrt{5}$: $\sqrt{6}$, etc., which confirmed the body-centered cubic (BCC) symmetry of the CD-MOF. After drug loading, the Bragg long period ($L = 2\pi/q_1$, 2.2 nm) of AZL/CD-MOF was unchanged as compared to parent CD-MOF. By contrast, the scattering behavior of free drug was different from the one of CD-MOF, with no apparent peak observed before q_5. However, all
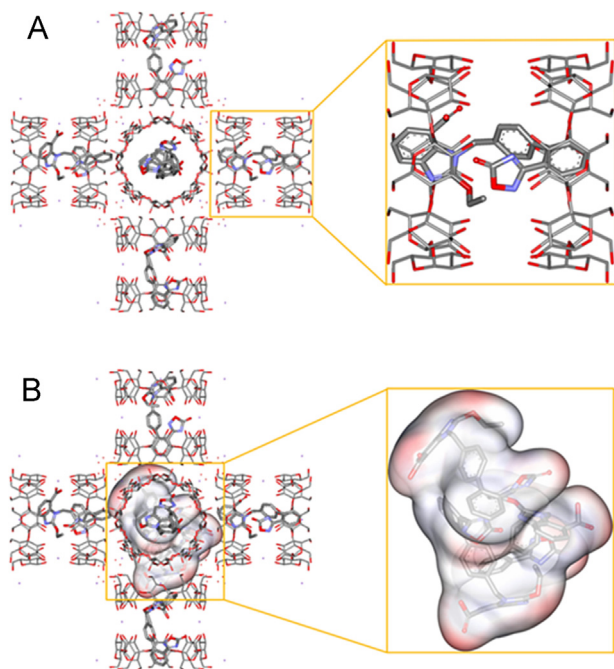
Figure 6 Conformation of AZL molecules distributed in CD-MOF: AZL integrated in the cavities of γ-CD pairs inside CD-MOF (A) and AZL assemblies as nanoclusters in the large cage-like confined space of CD-MOF (B). The red part indicated the strongest electronic donation region and the blue represented the strongest electronic acceptance region. (All the hydrogen atoms were omitted for the sake of clarity).

the peaks of AZL/CD-MOF were significantly shifted to higher fields, demonstrating that the diameters of cavities were reduced. In addition, the full width half maximum (FWHM) of CD-MOF increased after drug loading, which indicated that the degree of structural order decreased due to the incorporation of AZL. More importantly, the q_2 peak ($d = 2\pi/q_2$, diameter of 1.6 nm), which was considered as the signal of the largest cavities (theoretical diameter of 1.7 nm) in CD-MOF almost disappeared after AZL loading. This could be attributed to an occupation of the large CD-MOF cavities by the AZL molecules, leading to the signal change of CD-MOF in SAXS.

3.6. Mechanism of AZL distribution in CD-MOF by molecular docking

Molecular docking was employed to study the mechanism of the AZL distribution inside the CD-MOF. Herein, AutoDock used in this research is a semi-empirical free energy calculation method, based on the Lamarckian Genetic Algorithm (LGA) to search docking sites and Amber ForceField to evaluate the energy matching between the receptor and the ligand. The atoms of C, H, O and N in this article were included in the ForceField. The intramolecular energies were included in the formula for docking free energy. However, this term was always close to zero. The interactional free energy between AZL and CD-MOF mainly depends on the non-covalent interaction and other terms. Consequently, it should also give a better estimate for the absolute free energy[51,52]. The relative free energy was more reliable for the

comparison of the same system. Accordingly, the docking results are all reliable and meaningful for the discussion in this article. From a thermodynamic point of view, the conformations with the lowest free energy are the most stable one. Therefore, relatively low energy was used for energy optimization and molecular dynamics calculations in docking[31]. The results showed that AZL molecules preferred to stay in the hydrophobic cavities of γ-CD pairs (0.8 nm) rather than in the spherical cages of 1.7 nm of CD-MOF (Supporting Information Fig. S1). When the solution concentration of AZL was low or AZL molecules entered in CD-MOF at the beginning, it mainly distributed in the cavities of γ-CD pairs inside CD-MOF (Fig. 6A). The binding free energy in this case was -10.1 kcal/mol. Under such conditions, AZL molecules mainly existed in the γ-CD pairs inside CD-MOF with hydrophobic interactions, in which the hydroxyl groups of γ-CDs formed hydrogen bonds with AZL molecules. The hydrogen bonding was critical for the stabilization of the host-guest system[53,54]. Under the condition of higher concentration or the prolonged loading time, AZL molecules could exist in the cage-like confined space of CD-MOF. Three AZL molecules were shown to be packed as an assembly in the spherical cavity (Fig. 6B). The hydrophilic groups of AZL molecules were shown to be interacted with hydrophilic hydroxyl of the inside surface of CD-MOF cavity. The distribution of AZL molecules appeared to be chaotic at over concentration due to the limited cavity space so that unable to accommodate more AZL molecules. The experimental data of the maximum loading capacity as 1:1 molar ratio of AZL to γ-CD in CD-MOF had further confirmed that it is difficult for more than three AZL molecules to enter the large cavity of CD-MOF. Overall, confined nanometer-sized cage-like space could loosely accommodate three AZL molecules as assemblies of nanoclusters. When CD-MOF dissolved in water, the structure of CD-MOF will totally collapse and there are three forms of AZL in the solution system, one is γ-CD inclusion complex, one is free AZL and the other one is the nanocluster. The nanoclusters, which have uniform and tiny size immediately released from CD-MOF could temporarily increase the apparent solubility of AZL in water. It is also a "ship in a bottle" approach to form drug nanoclusters in CD-MOF. Herein, versatile CD-MOF was a carrier as well as a template formed nanocluster and γ-CD inclusion complex of AZL. Extra enhancement in bioavailability of AZL was subsequently obtained benefited from nanoclusters in the solution system.

4. Conclusions

In summary, CD-MOF has been investigated and validated as an efficient carrier to enhance the solubility and bioavailability of insoluble drug, a combined molecule mechanism of complexation and nanoclusterization has been proposed and experimentally verified, which is outclassed in CD-MOF drug delivery researches. Confirmed by experimental data either from the SR-FTIR, PXRD, SAXS and molecular docking, the high payload of AZL in CD-MOF relies on the formation of super tiny (1.7 nm) nanoclusters within CD-MOF, which is possibly one of the smallest nanoparticles of APIs can be made. Hence, the research suggested that CD-MOF is a highly potential and efficient form of nano drug delivery system for tailoring the bioavailability of poorly water-soluble drugs to its maximum.

Acknowledgments

Appendix A.   Supporting information

Supplementary data associated with this article can be found in the online version at https://doi.org/10.1016/j.apsb.2018.09.003.

References

1. Li B, Wen HM, Cui Y, Zhou W, Qian G, Chen B. Emerging multifunctional metal-organic framework materials. *Adv Mater* 2016;**28**:8819–60.
2. Kitagawa S, Kitaura R, Noro S. Functional porous coordination polymers. *Angew Chem Int Ed Engl* 2004;**43**:2334–75.
3. Howarth AJ, Peters AW, Vermeulen NA, Wang TC, Hupp JT, Farha OK. Best practices for the synthesis, activation, and characterization of metal–organic frameworks. *Chem Mater* 2017;**29**:26–39.
4. Xia W, Qu C, Liang Z, Zhao B, Dai S, Qiu B, et al. High-performance energy storage and conversion materials derived from a single metal-organic framework/graphene aerogel composite. *Nano Lett* 2017;**17**:2788–95.
5. Kreno LE, Leong K, Farha OK, Allendorf M, Van Duyne RP, Hupp JT. Metal-organic framework materials as chemical sensors. *Chem Rev* 2012;**112**:1105–25.
6. Wales DJ, Grand J, Ting VP, Burke RD, Edler KJ, Bowen CR, et al. Gas sensing using porous materials for automotive applications. *Chem Soc Rev* 2015;**44**:4290–321.
7. Mason JA, Veenstra M, Long JR. Evaluating metal-organic frameworks for natural gas storage. *Chem Sci* 2014;**5**:32–51.
8. Li JR, Kuppler RJ, Zhou HC. Selective gas adsorption and separation in metal-organic frameworks. *Chem Soc Rev* 2009;**38**:1477–504.
9. Hartlieb KJ, Holcroft JM, Moghadam PZ, Vermeulen NA, Algaradah MM, Nassar MS, et al. CD-MOF: a versatile separation medium. *J Am Chem Soc* 2016;**138**:2292–301.
10. Xu X, Wang C, Li H, Li X, Liu B, Singh V, et al. Evaluation of drug loading capabilities of gamma-cyclodextrin-metal organic frameworks by high performance liquid chromatography. *J Chromatogr A* 2017;**1488**:37–44.
11. Gascon J, Corma A, Kapteijn F. Llabrés i Xamena FX. Metal organic framework catalysis: *quo vadis*?. *ACS Catal* 2013;**4**:361–78.
12. Bui TT, Kim YS, Chun H, La DD, Bhosale SV. Template synthesis of micro/mesoporous Cl-doped polypyrrole using vapor phase polymerization. *Mater Lett* 2017;**192**:80–3.
13. Sun CY, Qin C, Wang XL, Su ZM. Metal-organic frameworks as potential drug delivery systems. *Expert Opin Drug Deliv* 2013;**10**:89–101.
14. Horcajada P, Chalati T, Serre C, Gillet B, Sebrie C, Baati T, et al. Porous metal-organic-framework nanoscale carriers as a potential platform for drug delivery and imaging. *Nat Mater* 2010;**9**:172–8.
15. Miller SR, Heurtaux D, Baati T, Horcajada P, Greneche JM, Serre C. Biodegradable therapeutic MOFs for the delivery of bioactive molecules. *Chem Commun* 2010;**46**:4526–8.
16. Ren F, Yang B, Cai J, Jiang Y, Xu J, Wang S. Toxic effect of zinc nanoscale metal-organic frameworks on rat pheochromocytoma (PC12) cells *in vitro*. *J Hazard Mater* 2014;**271**:283–91.
17. Baati T, Njim L, Neffati F, Kerkeni A, Bouttemi M, Gref R, et al. In depth analysis of the *in vivo* toxicity of nanoparticles of porous iron(iii) metal-organic frameworks. *Chem Sci* 2013;**4**:1597.
18. Lyu F, Zhang Y, Zare RN, Ge J, Liu Z. One-pot synthesis of protein-embedded metal-organic frameworks with enhanced biological activities. *Nano Lett* 2014;**14**:5761–5.
19. Hu Q, Yu J, Liu M, Liu A, Dou Z, Yang Y. A low cytotoxic cationic metal-organic framework carrier for controllable drug release. *J Med Chem* 2014;**57**:5679–85.
20. Smaldone RA, Forgan RS, Furukawa H, Gassensmith JJ, Slawin AM, Yaghi OM, et al. Metal-organic frameworks from edible natural products. *Angew Chem Int Ed Engl* 2010;**49**:8630–4.
21. Gu ZG, Li DJ, Zheng C, Kang Y, Woll C, Zhang J. MOF-templated synthesis of ultrasmall photoluminescent carbon-nanodot arrays for optical applications. *Angew Chem Int Ed Engl* 2017;**56**:6853–8.
22. Shegokar R, Muller RH. Nanocrystals: industrially feasible multifunctional formulation technology for poorly soluble actives. *Int J Pharm* 2010;**399**:129–39.
23. Li L, Liu Y, Wang JJ, Chen LJ, Zhang WJ, Yan XC. Preparation, *in vitro* and *in vivo* evaluation of bexarotene nanocrystals with surface modification by folate–chitosan conjugates. *Drug Deliv* 2016;**23**:79–87.
24. Lv N, Guo T, Liu B, Wang C, Singh V, Xu X, et al. Improvement in thermal stability of sucralose by gamma-cyclodextrin metal-organic frameworks. *Pharm Res* 2017;**34**:269–78.
25. Hartlieb KJ, Ferris DP, Holcroft JM, Kandela I, Stern CL, Nassar MS, et al. Encapsulation of ibuprofen in CD-MOF and related bioavailability studies. *Mol Pharm* 2017;**14**:1831–9.
26. Liu B, Li H, Xu X, Li X, Lv N, Singh V, et al. Optimized synthesis and crystalline stability of γ-cyclodextrin metal-organic frameworks for drug adsorption. *Int J Pharm* 2016;**514**:212–9.
27. Moussa Z, Hmadeh M, Abiad MG, Dib OH, Patra D. Encapsulation of curcumin in cyclodextrin-metal organic frameworks: dissociation of loaded CD-MOFs enhances stability of curcumin. *Food Chem* 2016;**212**:485–94.
28. Michel MC, Foster C, Brunner HR, Liu L. A systematic comparison of the properties of clinically used angiotensin II type 1 receptor antagonists. *Pharmacol Rev* 2013;**65**:809–48.
29. White WB, Weber MA, Sica D, Bakris GL, Perez A, Cao C, et al. Effects of the angiotensin receptor blocker azilsartan medoxomil versus olmesartan and valsartan on ambulatory and clinic blood pressure in patients with stages 1 and 2 hypertension. *Hypertension* 2011;**57**:413–20.
30. Ojima M, Igata H, Tanaka M, Sakamoto H, Kuroita T, Kohara Y, et al. *In vitro* antagonistic properties of a new angiotensin type 1 receptor blocker, azilsartan, in receptor binding and function studies. *J Pharmacol Exp Ther* 2011;**336**:801–8.
31. Lu T, Sun Y, Ding D, Zhang Q, Fan R, He Z, et al. Study on enhanced dissolution of azilsartan-loaded solid dispersion, prepared by combining wet milling and spray-drying technologies. *AAPS PharmSciTech* 2017;**18**:473–80.
32. Kawaguchi N, Ebihara T, Takeuchi T, Morohashi A, Yamasaki H, Tagawa Y, et al. Absorption of TAK-491, a new angiotensin II receptor antagonist, in animals. *Xenobiotica* 2013;**43**:182–92.
33. Angeli F, Verdecchia P, Pascucci C, Poltronieri C, Reboldi G. Pharmacokinetic evaluation and clinical utility of azilsartan medoxomil for the treatment of hypertension. *Expert Opin Drug Metab Toxicol* 2013;**9**:379–85.
34. Kalepu S, Nekkanti V. Insoluble drug delivery strategies: review of recent advances and business prospects. *Acta Pharm Sin B* 2015;**5**:442–53.
35. Shekhawat PB, Pokharkar VB. Understanding peroral absorption: regulatory aspects and contemporary approaches to tackling solubility and permeability hurdles. *Acta Pharm Sin B* 2017;**7**:260–80.
36. Ahire E, Thakkar S, Darshanwad M, Misra M. Parenteral nanosuspensions: a brief review from solubility enhancement to more novel and specific applications. *Acta Pharm Sin B* 2018. Available form: http://dx.doi.org/10.1016/j.apsb.2018.07.011.
37. Al-Kassas R, Bansal M, Shaw J. Nanosizing techniques for improving bioavailability of drugs. *J Control Release* 2017;**260**:202–12.

38. Clas SD, Sanchez RI, Nofsinger R. Chemistry-enabled drug delivery (prodrugs): recent progress and challenges. *Drug Discov Today* 2014;**19**:79–87.

39. El Khoury ED, Patra D. Ionic liquid expedites partition of curcumin into solid gel phase but discourages partition into liquid crystalline phase of 1,2-dimyristoyl-sn-glycero-3-phosphocholinesn liposomes. *J Phys Chem B* 2013;**117**:9699–708.

40. Paudel A, Worku ZA, Meeus J, Guns S, Van den Mooter G. Manufacturing of solid dispersions of poorly water soluble drugs by spray drying: formulation and process considerations. *Int J Pharm* 2013;**453**:253–84.

41. Li Z, Li H, Wang C, Xu J, Singh V, Chen D, et al. Sodium dodecyl sulfate/β-cyclodextrin vesicles embedded in chitosan gel for insulin delivery with pH-selective release. *Acta Pharm Sin B* 2016;**6**:344–51.

42. Lam S. Azilsartan: a newly approved angiotensin II receptor blocker. *Cardiol Rev* 2011;**19**:300–4.

43. Kamada T, Hayashi M, Fujiwara W, Yoshikawa D, Mukaide D, Sugishita Y, et al. Antihypertensive efficacy and safety of the angiotensin receptor blocker azilsartan in elderly patients with hypertension. *Drug Chem Toxicol* 2017;**40**:110–4.

44. Georgiopoulos G, Katsi V, Oikonomou D, Vamvakou G, Koutli E, Laina A, et al. Azilsartan as a potent antihypertensive drug with possible pleiotropic cardiometabolic effects: a review study. *Front Pharmacol* 2016;**7**:235.

45. Miura S, Saku K. Possible benefits of azilsartan compared with other angiotensin II type 1 receptor blockers. *Hypertens Res* 2014;**37**:799–800.

46. Zhang X-R, Zhang L. Solvent effect on the self-assembly of salt solvates of an antihypertensive drug azilsartan and 2-methylimidazole. *J Mol Struct* 2017;**1137**:320–7.

47. Trott O, Olson AJ. Software news and update AutoDock Vina: improving the speed and accuracy of docking with a new scoring function, efficient optimization, and multithreading. *J Comput Chem* 2010;**31**:455–61.

48. Gasteiger J, Hutchings MG, Christoph B, Gann L, Hiller C, Low P, et al. A new treatment of chemical reactivity: development of EROS, an expert system for reaction prediction and synthesis design. *Top Curr Chem* 1987;**137**:19–73.

49. Van Duong T, Goderis B, Van Humbeeck J, Van den Mooter G. Microstructure of pharmaceutical semicrystalline dispersions: the significance of polymer conformation. *Mol Pharm* 2018;**15**:629–41.

50. Goesten MG, Stavitski E, Juan-Alcañiz J, Martiñez-Joaristi A, Petukhov AV, Kapteijn F, et al. Small-angle X-ray scattering documents the growth of metal-organic frameworks. *Catal Today* 2013;**205**:120–7.

51. Huey R, Morris GM, Olson AJ, Goodsell DS. A semiempirical free energy force field with charge-based desolvation. *J Comput Chem* 2007;**28**:1145–52.

52. Trott O, Olson AJ. AutoDock Vina: improving the speed and accuracy of docking with a new scoring function, efficient optimization, and multithreading. *J Comput Chem* 2010;**31**:455–61.

53. Sun M, Wu C, Fu Q, Di D, Kuang X, Wang C, et al. Solvent-shift strategy to identify suitable polymers to inhibit humidity-induced solid-state crystallization of lacidipine amorphous solid dispersions. *Int J Pharm* 2016;**503**:238–46.

54. Sun M, Li B, Li Y, Liu Y, Liu Q, Jiang H, et al. Experimental observations and dissipative particle dynamic simulations on microstructures of pH-sensitive polymer containing amorphous solid dispersions. *Int J Pharm* 2017;**517**:185–95.